Turbulence Variations in the Upper Troposphere in Tropical Cyclones from NOAA G-IV Flight-Level Vertical Acceleration Data

JOHN MOLINARI

Department of Atmospheric and Environmental Sciences, University at Albany, State University of New York, Albany, New York

MICHAELA ROSENMAYER

World Fuel Services, Miami, Florida

DAVID VOLLARO AND SARAH D. DITCHEK

Department of Atmospheric and Environmental Sciences, University at Albany, State University of New York, Albany, New York

(Manuscript received 8 June 2018, in final form 4 January 2019)

ABSTRACT

The NOAA G-IV aircraft routinely measures vertical aircraft acceleration from the inertial navigation system at 1 Hz. The data provide a measure of turbulence on a 250-m horizontal scale over a layer from 12.8- to 14.8-km elevation. Turbulence in this layer of tropical cyclones was largest by 35%–40% in the inner 200 km of radius and decreased monotonically outward to the 1000-km radius. Turbulence in major hurricanes exceeded that in weaker tropical cyclones. Turbulence data points were divided among three regions of the tropical cyclone: cirrus canopy; outside the cirrus canopy; and a transition zone between them. Without exception, turbulence was greater within the canopy and weaker outside the canopy. Nighttime turbulence exceeded daytime turbulence for all radii, especially within the cirrus canopy, implicating radiative forcing as a factor in turbulence generation. A case study of widespread turbulence in Hurricane Ivan (2004) showed that interactions between the hurricane outflow channel and westerlies to the north created a region of absolute vorticity of $-6 \times 10^{-5}\,s^{-1}$ in the upper troposphere. Outflow accelerated from the storm center into this inertially unstable region, and visible evidence for turbulence and transverse bands of cirrus appeared radially inward of the inertially unstable region. It is argued that both cloud-radiative forcing and the development of inertial instability within a narrow outflow layer were responsible for the turbulence. In contrast, a second case study (Isabel 2003) displayed strong near-core turbulence in the presence of large positive absolute vorticity and no local inertial instability. Peak turbulence occurred 100 km downwind of the eyewall convection.

1. Introduction

Turbulence in tropical cyclones

Molinari et al. (2014, hereafter MDV14) and Duran and Molinari (2016) described the vertical variation of the bulk Richardson number R_B in tropical cyclones using both rawinsondes and G-IV dropsondes. Figure 1 shows the vertical profile of the fraction of rawinsonde observations within 500 km of a major hurricane that contained $R_B < 1$ and $R_B < 0.25$. The latter regions were most likely to contain turbulence. A peak in the frequency of low Richardson numbers existed in the planetary boundary layer, as expected. A clear secondary maximum, however, occurred in the upper troposphere, in the layer containing the tropical cyclone cirrus canopy (e.g., Cairo et al. 2008). Low R_B layers fell into three broad groups. The most common was located within cirrus canopy clouds in the upper troposphere (centered above 13 km) and was due almost entirely to low static stability layers within the cirrus deck. The authors speculated that these were produced by longwave and shortwave radiative forcing within the upper-tropospheric cirrus. The second type of low R_B was found below the cloud base near the

Corresponding author: John Molinari, jmolinari@albany.edu

DOI: 10.1175/JAMC-D-18-0148.1

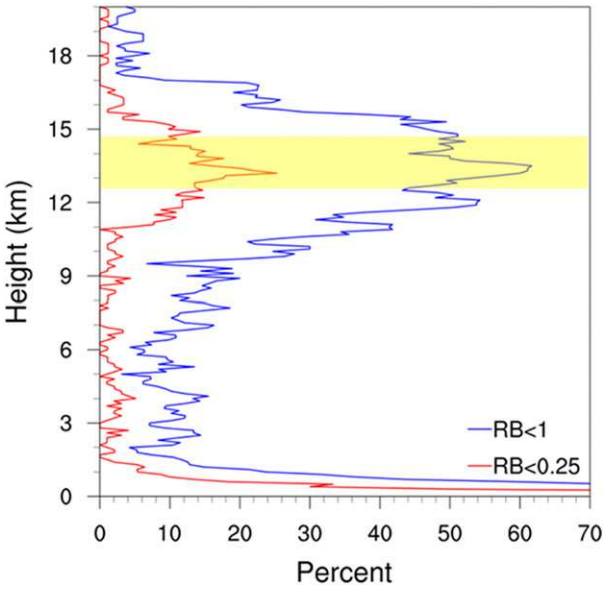

FIG. 1. Percentage of rawinsondes having $R_B < 1$ (blue) and $R_B < 0.25$ (red), calculated from the surface to the 20-km elevation from 96 rawinsondes within 500 km of 17 major hurricanes (Fig. 4 from MDV14). The yellow shading indicates the layer in which G-IV VAA data are examined.

edge of the cirrus canopy, most commonly occurring at 9–10-km height, where relative humidity fell below 40%. Near-zero static stability existed within the turbulent layer, with stability and shear maxima above it. This structure strongly resembled that seen previously from sublimation of precipitation beneath cirrus (Luce et al. 2010; Kudo 2013). The third type of turbulent layer existed mostly outside the cirrus canopy and was produced by large local vertical wind shear beneath the outflow jet. The results suggest the cirrus canopy in tropical cyclones creates its own distinctive stability and shear profiles that strongly influence the distribution of turbulence. The results supported the closure of Emanuel and Rotunno (2011) and Emanuel (2012), whose theoretical model required the Richardson number to be near a critical value for turbulence in the outflow layer.

Several excellent review papers have been written on turbulence in the atmosphere (Knox et al. 2010; Sharman et al. 2012; Lane et al. 2012). Upper-tropospheric turbulence is generated by overshooting convection, and peaks about 1 km above the convection. A second type of turbulent region propagates away from the convection, and owes its existence to shear and stability variations forced by convectively driven gravity waves (e.g., Lane et al. 2012). This can produce alternating layers of low and high Richardson numbers more than 100 km from the convection. Gravity waves have been observed and simulated in tropical cyclones (Pfister et al. 1993; Kuester et al. 2008). The waves had a 15–100-km horizontal wavelength, a 4–8-km vertical wavelength, and 20–100-min periods. The waves in the study of Pfister et al. (1993) appeared to be driven by mesoscale heating regions moving within the tropical cyclone. These large-amplitude, localized gravity waves appear to be relatively rare, asymmetric, and episodic. Smaller-scale, high-frequency, nearly continuous gravity waves in the lower troposphere were simulated by Nolan and Zhang (2017). Those waves near 700 hPa were beneath the layer of interest in this study.

Sublimation of ice beneath precipitating cirrus also produces turbulence, supported both by observations in a region of cirrus (not associated with a tropical cyclone; Luce et al. 2010) and high-resolution idealized modeling of precipitating cirrus (Kudo 2013). In these studies, turbulent layers extended downward by as much as 2 km beneath the sublimation layer, but not above, because of the presence of strong stability maxima. MDV14 show several examples of this phenomenon in tropical cyclones.

Other than the data collected by the G-IV aircraft, direct measurements of turbulence are rare in the upper troposphere of tropical cyclones. By making use of commercial pilot reports, Kim et al. (2014) found regions of moderate and severe turbulence near $z = 12$ km in a Pacific typhoon undergoing extratropical transition. The turbulence occurred several hundred kilometers away from the center within the anticyclonic outflow layer. The turbulent regions were characterized by banded structures within the cirrus cloud shield. Such bands might be associated with small Richardson numbers, but also with the presence of negative absolute vorticity (Knox et al. 2010), which in tropical cyclones is most likely in the outflow layer (Rappin et al. 2011; Ditchek et al. 2017). In an overview of the existence of cirrus bands in tropical cyclones, Knox et al. (2010) noted a 10–50-km spacing between the bands, which were oriented like spokes on a wheel at the edges of the cirrus canopy. Pilots avoid such bands, which are known to be turbulent (e.g., Lenz et al. 2009; Knox et al. 2010). Kim et al. (2014) simulated turbulent cirrus bands in a tropical cyclone. They argued that cloud-radiative forcing and large vertical wind shear each contributed to the formation of the observed bands. Trier and Sharman (2009) and Trier et al. (2010) found similar mechanisms in the outflow layer of mesoscale convective systems over land.

Duran and Molinari (2019) found that turbulence had a substantial influence on upper-tropospheric stability in tropical cyclones. Surprisingly, turbulence was shown to produce maxima and minima in static stability in a high-resolution numerical model. This arose because the magnitude of turbulence changed dramatically with height in a manner that was consistent with vertical

gradients of Richardson numbers. The changing static stability fields altered the shape of the transverse circulation and strongly influenced the upper-tropospheric potential vorticity. Turbulence played a significant role in this evolution.

Light-to-moderate turbulence occurs at times during every NOAA G-IV flight, especially when the aircraft is within or above cirrus (J. Kaplan 2017, personal communication). The G-IV aircraft routinely measures instantaneous vertical aircraft acceleration (VAA) from the Inertial Navigation System (INS) at 1 Hz, equivalent to a 250-m horizontal scale. In this paper the term ''turbulence'' is used to describe the absolute value of VAA on that scale. This dataset is, to our knowledge, the only measure of turbulence over large spatial regions of multiple tropical cyclones, whereas previous work was more anecdotal.

Given the evidence for the important roles of turbulence in the above papers, the goals of this paper are (i) to describe the distribution of turbulence with respect to storm intensity, radius, and time of day and (ii) make use of these distributions to gain insight into the thermodynamics (role of clouds and radiation) and dynamics (inertial instability) within the tropical cyclone outflow layer. In addition, brief case studies provide detail for two specific storms: Hurricanes Ivan (2004) and Isabel (2003). These provide insight into the influences of variations in the storm environment on the distribution of turbulence.

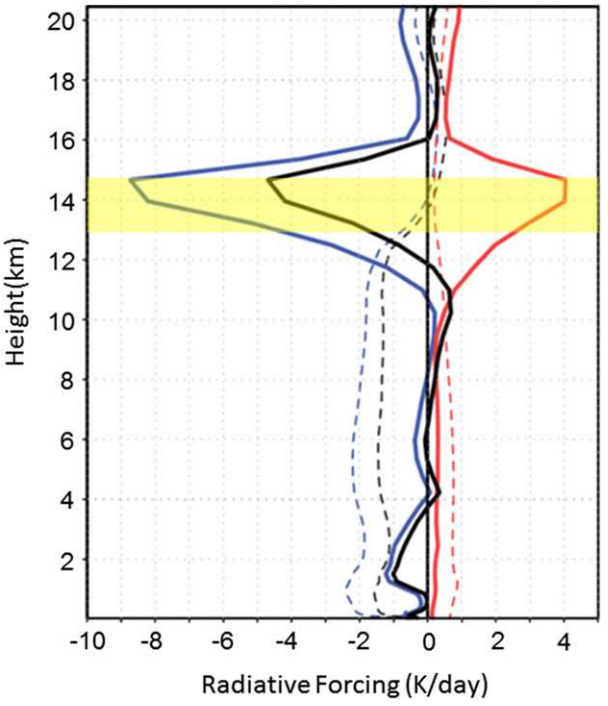

FIG. 2. The area-averaged vertical profiles of the radiative forcing tendencies (Fig. 7c of Bu et al. 2014). Given are longwave (blue) and shortwave (red) radiative heating, and their sum (black). Solid lines indicate the mean over 350-km radius in a tropical cyclone; dashed lines indicate the same fields from the RRTMG clear-sky sounding. The yellow shading is as in Fig. 1.

2. Radiative forcing in tropical cyclones

Figures 2 and 3 have been adapted from Bu et al. (2014), who evaluated the role of radiative forcing in multiple idealized numerical model simulations of tropical cyclones. The yellow bar represents the G-IV flight-level range. Figure 2 displays, averaged over the diurnal cycle, shortwave radiative warming and longwave warming and cooling using the HWRF numerical model with Thompson et al. (2008) microphysics and Rapid Radiative Transfer Model for Global Circulation Models (RRTMG) radiation (Fig. 7c from Bu et al. 2014). The dashed lines represent undisturbed clear skies, and the solid lines show the cloudy region of the tropical cyclone. The clear-sky net radiative forcing arose because longwave cooling exceeded the diurnal mean of shortwave warming, creating about $1\,\mathrm{K\,day^{-1}}$ net radiative cooling without much vertical variation below 12-km height.

The presence of a tropical cyclone cirrus canopy substantially altered the net forcing. In the cloudy regions, longwave cooling began near 10-km height and intensified steadily to a value of $-9\,\mathrm{K\,day^{-1}}$ at 14.5-km height. Shortwave warming peaked in the same layer, but with a smaller magnitude. As a result, averaged over the day, significant net cooling existed in the cirrus canopy between 13 and 15 km. Other things being equal, such forcing reduces the static stability beneath the peak cooling. It is striking that the greatest frequency of low R_B (Fig. 1) was found in the same region. This suggests a significant role for radiative forcing in producing turbulence in tropical cyclones.

The radius–height distribution of azimuthally averaged cloud condensate (shading) and net radiative warming (contours) over the length of the day is given in Fig. 3 [from Fig. 11a of Bu et al. (2014), which made use of a different high-resolution model and physical parameterizations than in Fig. 2, but with very similar results]. It is notable that the vertical gradient of cooling near the edge of the cirrus canopy exceeded that at inner radii. The difference arose not only from slightly stronger longwave cooling near 14-km elevation, but also stronger longwave warming that occurred near the 12-km height. Such a feature was found by Dinh et al. (2010) in thin and even in subvisible cirrus. In tropical cyclones near the edge of the cirrus canopy, where low- and middle-level cloudiness is less common, it is possible that blackbody radiation reaches the cirrus from the

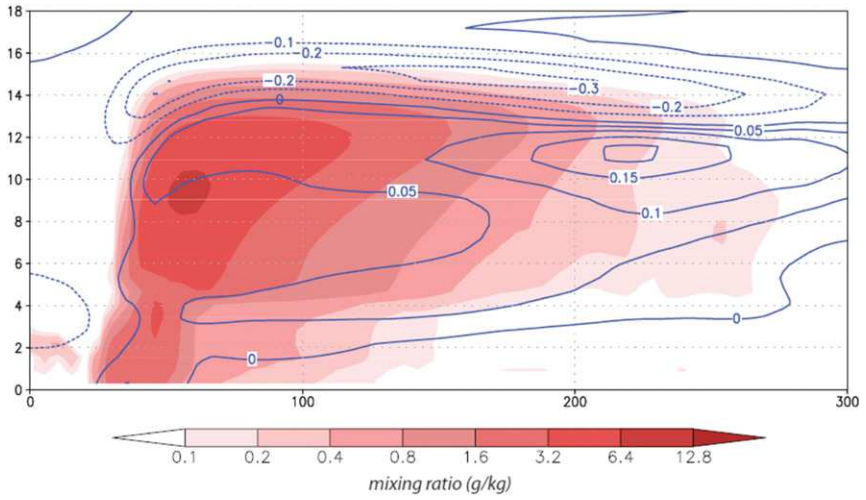

FIG. 3. Vertical cross section of the net azimuthally averaged longwave plus shortwave radiative heating averaged over a full day (adapted from Fig. 11a of Bu et al. 2014). Solid and dashed contours represent positive and negative heating rates, respectively. The total condensate is shaded on a log scale, and the net radiative heating is contoured (increment 0.05° h^{-1} for positive values and 0.1° h^{-1} for negative values).

warm ocean underneath. The net result is stronger radiative forcing at the cirrus canopy edge than at other radii. A great benefit of the turbulence data in this paper is its concentration in the layers of greatest interest for radiative forcing.

Melhauser and Zhang (2014) simulated tropical cyclones in the WRF model for perpetual day and perpetual night. Although they used a different numerical model and parameterized microphysics, their results supported Bu et al. (2014). Perpetual night simulations produced more intense convection and stronger storms as a result of destabilization by cloud-top cooling, consistent with Figs. 2 and 3. Perpetual daytime simulations produced substantial warming from 9 to 13 km and little net cloud-top cooling, resulting in weaker convection and weaker storms. Thus, although radiative forcing is smaller in magnitude than latent heating in a tropical cyclone, it still has a substantial impact, especially in the upper troposphere where heating associated with phase changes of water is much smaller than at lower levels. Figures 2 and 3 show that the vertical distribution of turbulence data from the G-IV aircraft is almost perfectly positioned to study these processes.

3. Data and methods

a. Turbulence data

Flight-level vertical acceleration of the G-IV aircraft at 1 Hz has been stored since 1998, but has not been examined to the authors' knowledge. NOAA Aircraft Operations Center (AOC) flight-level data are described at https://data.nodc.noaa.gov/cgi-bin/iso?id=gov.noaa.ncdc:C00581. The data are available at https://seb.noaa.gov/pub/acdata/. All Atlantic Ocean basin G-IV flights within 1000 km of the storm center from 1998 to 2016 are utilized for this study. Density changes were neglected over the narrow layer of interest. No systematic evidence of turbulence changes during aircraft turning were seen, and no data were removed during turns. Table 1 shows the distribution of the number of G-IV VAA observations within 1000 km of a tropical cyclone as a function of height over 400-m layers. The choice of 400 m minimized roundoff error and ensured stable vertical structure (see discussion by MDV14). Data are rare beneath 12.8 km and nonexistent above 14.8 km. The radial variation of turbulence is examined only for those layers with more than 300 000 observations, resulting in nearly 5 million VAA observations summed from 12.8 to 14.8 km. The G-IV turbulence data lie almost exclusively beneath the tropopause, which occurs in tropical cyclones within

TABLE 1. Number of 1-Hz G-IV VAA data points within 1000 km of tropical cyclones, separated into 400-m vertical layers.

Layer (km)	No. of VAA observations
12.0–12.4	20 371
12.4–12.8	24 725
12.8–13.2	335 779
13.2–13.6	1 058 894
13.6–14.0	1 094 716
14.0–14.4	1 684 672
14.4–14.8	786 755
14.8–15.2	0

the 15–18-km layer (Cairo et al. 2008; Molinari and Vollaro 2014; Duran and Molinari 2018, 2019).

Vonich and Hakim (2018) produced power spectral composites using lower-tropospheric flight-level data from the NOAA P-3 and the U. S. Air Force. They found that the spectral slope steepens over wavelengths of 10–200 km, and they suggested that analyses of spectra could ultimately provide more information on turbulence. The G-IV flight-level winds are not quality controlled, and thus such a potentially insightful calculation is not possible in this paper.

Data for radial variations of turbulence were organized into 200-km radial bins out to 1000 km. Only 7.2% of all turbulence observations within $r = 1000$ km existed within the 200-km radius, and 15% existed from 800- to 1000-km radii. The peak observation frequency was found almost uniformly from 200- to 800-km radii, amounting to 78% of the total.

Turbulence observations were separated into daytime (0600–1800 LT) and nighttime (1800–0600 LT). During most of the hurricane season, the daytime is longer than 12 h. At 0600 and 1800 LT, however, the sun angle is low, and radiative cooling is likely exceeding solar heating. Thus, even though the sun rises before 0600 LT and sets after 1800 LT in most storms, it was felt that the even split of the day into two 12-h periods was reasonable.

Examination of the magnitude of turbulence averaged over each season produced an artifact. The years from 2008 to 2013 contained nearly 50% higher mean turbulence magnitude than all years before and after that period. We normalized the outlier years to have the same mean as the other years. The appendix describes the nature of the problem and the resultant solution.

Statistically significant turbulence variations make use of the *t* test at the 99.999% level. The high significance threshold takes into account the large number of data points.

b. Other data

The cirrus canopy state at the location of each turbulence observation was defined using infrared brightness temperatures T_b. Only IR images within 15 min of observation times were used. This method has a weakness: as the cirrus thins it becomes partially transparent to infrared radiation, and the satellite senses warmer temperatures from below. This likely produces an unrealistically high T_b in the presence of thin cirrus. Given this weakness, very broad definitions of the cirrus state were employed. The cirrus canopy was defined as the region with $T_b < -40$°C. Regions without high cloud outside the canopy were represented by $T_b > 0$°C. A transition region was defined by brightness temperatures between 0° and −40°C. Figure 4 shows two examples of the cirrus canopy definition

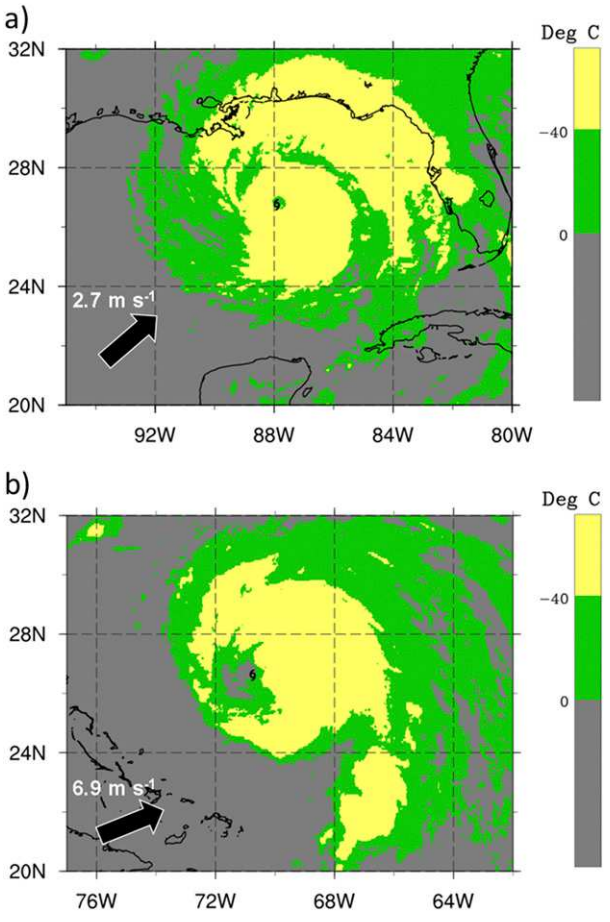

FIG. 4. Two examples of cirrus canopy definition: (a) 1215 UTC 15 Sep 2004 in Hurricane Ivan; (b) 0945 UTC 16 Sep 2003 in Hurricane Isabel. Yellow represents the cirrus canopy, gray represents outside the canopy, and green represents the transition region. The bold arrow and adjacent number provide vertical wind shear direction and magnitude between 850 and 200 hPa. Each of these time periods is addressed further in section 5.

resulting from this classification. These particular examples (from Hurricanes Ivan 2004 and Isabel 2003) were chosen because they are discussed in another context in section 5, which shows additional fields.

The radius for each observation was calculated using the great circle distance from HURDAT2 center positions (Landsea and Franklin 2013). HURDAT2 was first interpolated from 6-h to 1-min frequency in order to avoid unrealistic jumps in the center position in adjacent 1-Hz data.

The case studies made use of wind and absolute vorticity from ERA-Interim analyses (Dee et al. 2011) on a 0.7° × 0.7° grid. They also utilized G-IV dropsonde data described in detail by MDV14. Finally, vertical wind shear data every 6 h were obtained from the Statistical Hurricane Intensity Prediction Scheme (SHIPS). Shear was calculated in SHIPS as the magnitude difference

between 850- and 200-hPa wind vectors, averaged over a 0–500-km radius from the vortex center (DeMaria et al. 2005).

4. Results

The vertical aircraft acceleration varied with a near-normal distribution (Fig. 5a). Turbulence is the absolute value of VAA; the 99th percentile of turbulence was 0.43 m s^{-2} (Fig. 5b), but note that this does not represent extreme conditions. This lack of strong turbulence reflects in part the infrequent sampling of storm cores by the G-IV aircraft. Turbulent kinetic energy is often calculated using 25-Hz data, and no such resolution exists in the G-IV data. Of primary interest in this paper are the insights that the spatial variation of turbulence on a 250-m scale might provide about upper-tropospheric physics in tropical cyclones.

Both the major tropical cyclones and all other tropical cyclones from tropical depression to category 2 (Fig. 6a) showed peak turbulence at the innermost radial bin, 35%–40% larger than at outer radii. This is consistent with the large frequency of Richardson numbers below 0.25 at small radii in hurricanes and its outward decrease as shown by Duran and Molinari (2016). Major hurricanes exhibited 8% higher turbulence values at inner radii than weaker storms (Fig. 6a).

Nighttime turbulence exceeded that in daytime (Fig. 6b) by 9.9% at the 200–400-km radius and 7.6% in the inner 200 km. These radii are likely within the cirrus canopy (Fig. 4). Turbulence is larger overnight for all radii out to 1000 km.

Turbulence was separated into quadrants according to vertical wind shear direction in Fig. 6c. Turbulence peaked downshear left (DSL). DSL turbulence exceeded the opposite upshear right (USR) quadrant by 30% in the storm core. In general, downshear turbulence exceeded upshear, consistent with the variations of lightning with vertical shear given by Corbosiero and Molinari (2002). Cirrus canopies in sheared storms are asymmetric and favored downshear (e.g., Fig. 4).

The variation of turbulence with cloud type (Fig. 7a) shows the largest turbulence existed in the cirrus canopy outside the 200-km radius. From 200- to 400-km radii, the canopy region turbulence exceeded that from the transition region by 10.6% and the region outside the canopy by 17.5%. Figure 7a represents all times of day. Based on previous discussion (see the introduction and Fig. 6b), more turbulence is expected at night. Figure 7b compares turbulence in the cirrus canopy for night versus day. Nighttime turbulence exceeded daytime by 22.4% at the 200–400-km radius. The existence of deep cirrus appeared to play a significant role in the distribution of turbulence. The following section addresses selected case studies from individual storms.

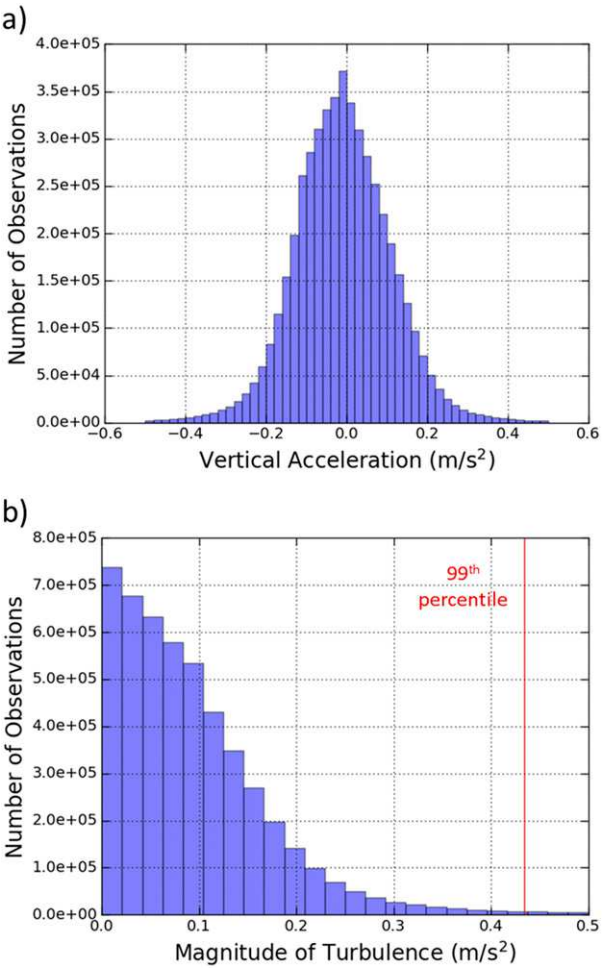

FIG. 5. Distribution of (a) VAA and (b) turbulence (absolute value of VAA; both in m s^{-2}) over all storms and radii. The 99th percentile value of 0.43 is given by the vertical line in (b).

5. Selected case studies

a. *Cirrus bands in Hurricane Ivan (2004)*

Hurricane Ivan (2004) was a Cape Verde–type storm that crossed the Atlantic, Caribbean, and Gulf of Mexico, and reached Category 5 intensity three separate times. The history of Hurricane Ivan is described in the National Hurricane Center report of the storm (https://www.nhc.noaa.gov/data/tcr/AL092004_Ivan.pdf). MDV14 examined R_B distributions in Ivan, and Molinari and Vollaro (2014) discussed the existence of symmetric instability in Ivan using a composite of 320 dropsondes released by the NOAA G-IV over several days. In this paper, only the G-IV flight on 15 September 2004 is addressed. Hurricane Ivan maximum winds

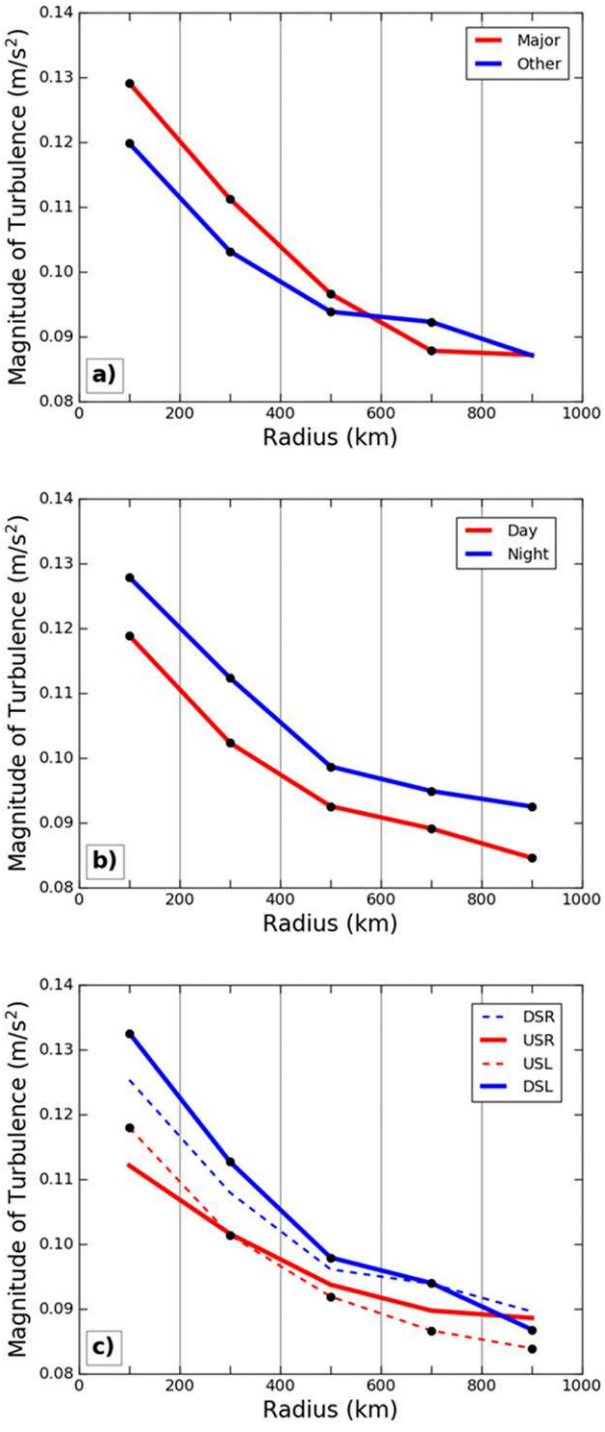

FIG. 6. (a) Radial variation of the mean turbulence magnitude ($m\,s^{-2}$) for major hurricanes (red) and all other tropical cyclones (blue) in 200-km radial increments. (b) As in (a), but for day (0600–1800 LT; red line) and night (1800–0600 LT; blue line). (c) As in (a), but for each of the four vertical wind shear–related quadrants, for all radii and times. DSL, DSR, USL, and USR refer to downshear left and right, and upshear left and right. Radii with black dots passed the significance test between the fields in (a) and (b) and between DSL and USL quadrants in (c).

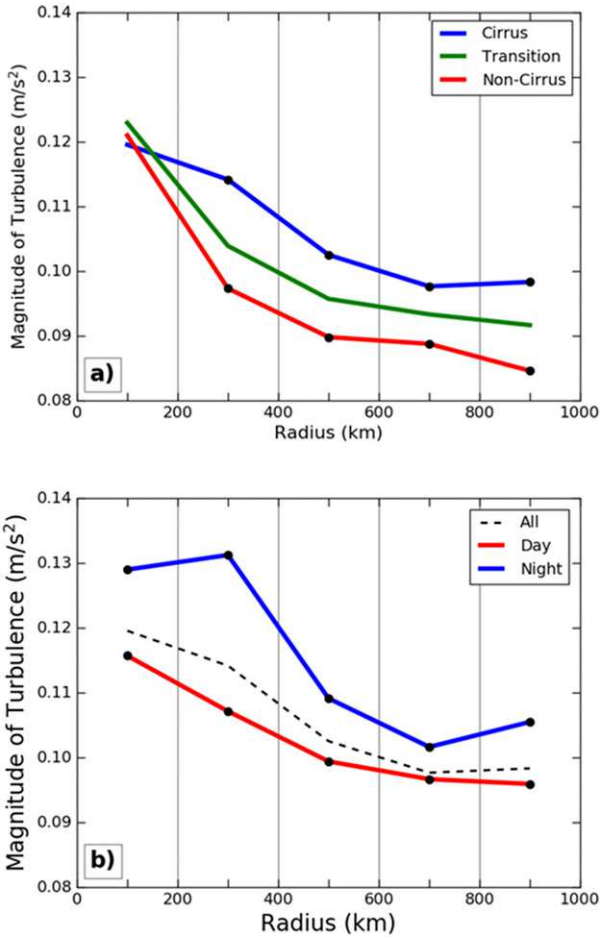

FIG. 7. (a) Magnitude of turbulence with respect to radius within the cirrus canopy (blue), in the transition zone (green), and outside the cirrus canopy (red). (b) Mean turbulence within the cirrus canopy only, separated into day and night. Dots indicate significant differences between cirrus and noncirrus in (a) and between night and day in (b). The black dashed line is the weighted mean of night and day.

weakened from 140 kt (1 kt $\approx$ 0.51 $m\,s^{-1}$) on the previous day to 115–120 kt over 24 h. Vertical wind shear evolved from 300° at 6.8 $m\,s^{-1}$ at 0000 UTC 15 September to 228° at 4.1 $m\,s^{-1}$ at 1200 UTC. The shear direction thus had a component from the west over the 12-h period.

An infrared image centered on the G-IV flight times is provided in Fig. 8. Also given are the flight track and the observations with turbulence greater than 0.43 $m\,s^{-2}$ (99th percentile, shown by white dots). The colored segments of the flight track are repeated in the lower panel. The black star is the initial time the G-IV reached the minimum altitude examined in this study. G-IV sonde locations are shown by the X's, except for soundings that are plotted in this paper, which are labeled A, B,

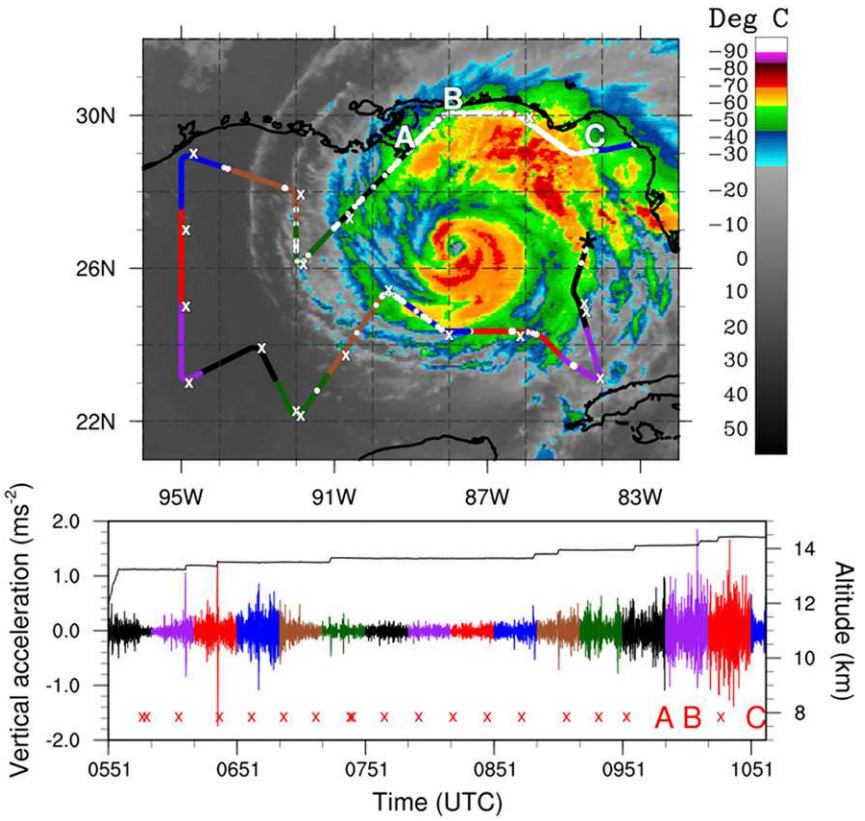

FIG. 8. (top) The G-IV flight track from 0551 to 1058 UTC 15 Sep 2004, overlaid onto infrared brightness temperature, analogous to Fig. 1 of Duran and Molinari (2016). This satellite image is valid at 1015 UTC, which lies within 2 h of the release of sondes A, B, and C. The locations with turbulence greater than 0.43 m s^{-2} (99th percentile) are shown by white dots. The track is divided into colored segments that are repeated in the lower panel, which displays the 1-Hz VAA values. The black star in the top panel gives the location where the G-IV first reached an altitude covered by this study. G-IV sonde locations in both panels are shown by the X marks (shifted off the track for clarity), except for soundings that are displayed, which are labeled A, B, and C. The sonde between B and C was not used because of a complete lack of wind data.

and C.[1] A time series of 1-Hz vertical aircraft acceleration values are plotted in the lower panel, along with the release times of the sondes.

Cloudiness was asymmetric in Hurricane Ivan at this time, with deep cirrus extending downshear and DSL of the storm (Fig. 4a). The aircraft flew at the outer edge of the regions of lower T_b. Two primary regions of turbulence existed, one south of the storm early in the flight, and the other north of the storm in the deep cirrus. This northern event will be examined further. Because of the 250-m resolution of the data, turbulence at the 99th percentile was not continuous in space to the north as implied by the nearly solid white line in Fig. 8. Instead, it occurred in 12.3% of points along the track between 84° and 90°W, which is 12 times larger than a 99th percentile frequency for the entire dataset, and 4 times larger than the average frequency in this Ivan flight. This region of Hurricane Ivan represented among the greatest concentration of turbulence outside the core for the storms that were examined.

Figure 9 shows soundings from three dropsondes north of the center. The sonde data begin 600 m beneath the aircraft (to allow adjustment to the environment of the sonde), and thus cannot directly address the source of flight-level turbulence above. However, winds and stability from the sondes will provide some insight. The magenta bars in Fig. 9 indicate 400-m thick layers in which $R_B < 0.25$, following MDV14. To the left of the soundings are the two components of R_B: stability in black and shear squared in green. Sonde A, at a radius 308 km north-northwest of the center, displayed

[1] The sonde between B and C was not used because of a complete lack of wind data.

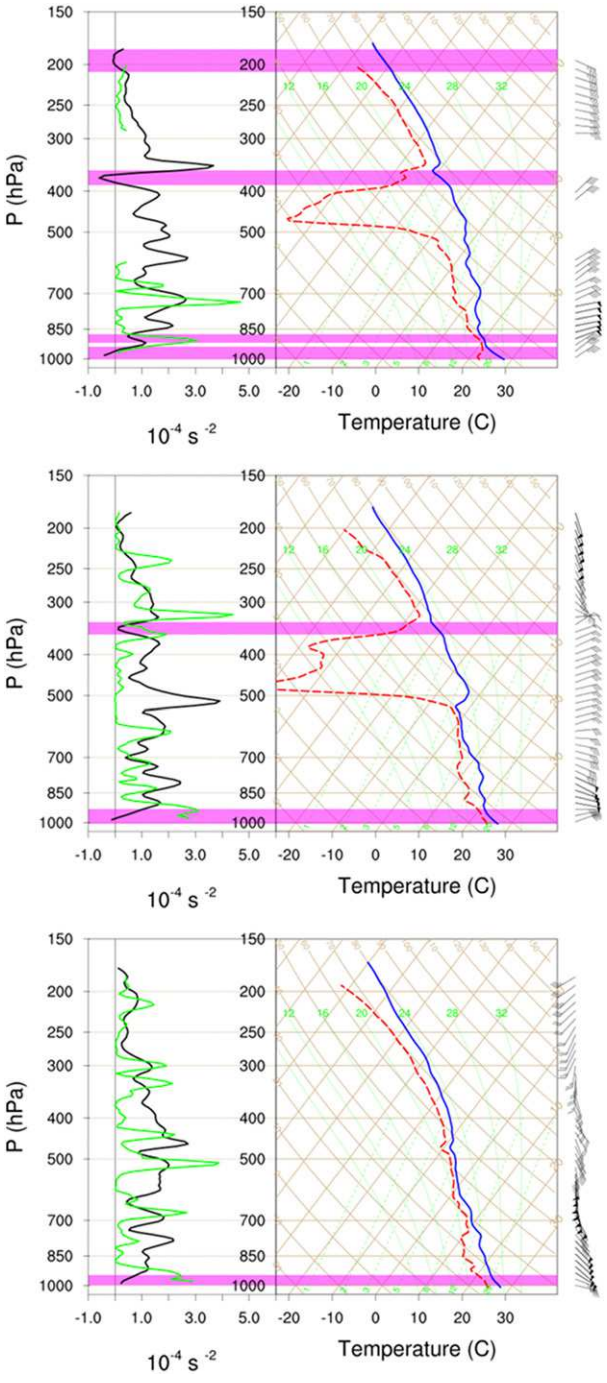

FIG. 9. Soundings from sondes (top) A, (middle) B, and (bottom) C. (left) Vertical profiles of the stability term (black; $10^{-4}\,s^{-2}$) and the shear squared term (green; $10^{-4}\,s^{-2}$) from the R_B definition. (right) Skew T–log$p$ diagrams for each sonde; solid blue shows temperature, and dashed red shows dewpoint. Each long wind barb is 5 m s^{-1}, and each short barb is 2.5 m s^{-1}. The magenta bands show the turbulent layers within the soundings, defined by $R_B < 0.25$.

multiple layers of $R_B < 0.25$.[2] The likely turbulent layer at 375 hPa in sonde A closely resembled those described by MDV14 and was caused by sublimation of precipitation beneath the cloud base. Consistent with this was very dry air beneath a well-defined cirrus base near 350 hPa and negative static stability just below the inferred sublimation layer. The presence of a capping inversion situated just above the sublimation layer and located well below the altitude of the aircraft suggests that these features are unlikely to influence the turbulence studied in this paper. Sublimation signatures in sondes are thus not explicitly addressed in subsequent soundings. A possible indirect role of sublimation is addressed in the discussion. More relevant to the flight-level turbulence observed in Fig. 9 is an unstable layer in sonde A at the top of the sounding, which lies about 600 m beneath flight level. MDV14 attributed such layers to destabilization by longwave cooling increasing upward and reducing static stability.

Sonde B was located almost directly north of the storm at the 404-km radius. The cirrus base remained well defined near 350 hPa. Outflow reached 25 m s^{-1} at the top of sonde B, where tangential winds were weak. This is suggestive of the results of MDV14 and Molinari and Vollaro (2014), who found enhanced outflow in Ivan where inertial stability was weak.

Sonde C was found to the east of the turbulent layer. Its structure dramatically differed from the others, containing a nearly saturated column and no sublimation signature. Static stability was higher than for the other sondes. Anticyclonic outflow occurred at the top of the sounding, but the outflow was weaker than for sonde B.

The cloud distribution was somewhat disrupted and banded north of the storm at 1215 UTC 15 September (Fig. 4a). Infrared images, however, often do not show cirrus bands clearly (Lenz et al. 2009). Figure 10 provides visible satellite images and absolute vorticity and wind vectors at 175 hPa near 0000 and 1200 UTC 15 September. Some striking changes occurred over this 12-h period. At 0000 UTC (Fig. 10a), absolute vorticity north of the storm reached $-6 \times 10^{-5}\,s^{-1}$. This represents strong local inertial instability. The negative absolute vorticity existed north of an arc of very small-scale cloud fluctuations near 27.5°N near the northern edge of the main cirrus canopy. By 1200 UTC (Fig. 10b), no negative absolute vorticity was found

[2] The unstable layer just above 400 hPa was labeled even though winds were not available in that layer. Static stability is negative, however, and shear is zero or positive, and thus R_B must be zero or negative.

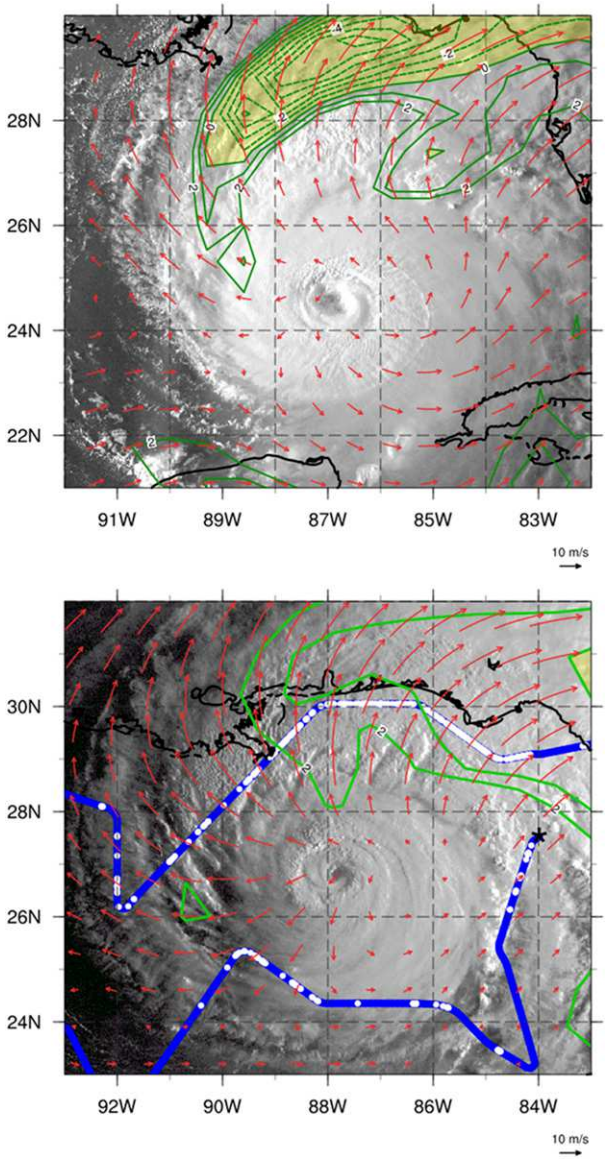

FIG. 10. Visible images valid at (top) 2245 UTC 14 Sep and (bottom) 1215 UTC 15 Sep (same time as Fig. 4a). Absolute vorticity (yellow shading for negative values and contoured in green; increment $1 \times 10^{-5}\,s^{-1}$) and winds at the 175-hPa level are also shown at 0000 and 1200 UTC 15 Sep. Only absolute vorticity values below $2 \times 10^{-5}\,s^{-1}$ are shown to avoid dense contours near the storm core. In the lower panel the blue G-IV flight track also shows the locations of turbulence above the 99th percentile in white dots.

near the storm center, indicating a dramatic response to the previous instability. The representation of the convection seemed to change somewhat, from cellular near 0000 UTC to banded at 1200 UTC near 29°N. The cirrus bands shifted northward with the storm. The presence of turbulence in such bands is consistent with the review of Knox et al. (2010).

b. *Near-core turbulence in Hurricane Isabel (2003)*

Hurricane Isabel was a long-lived Cape Verde–type storm that reached category 5 status during its traverse of the Atlantic and made landfall in North Carolina as a category 2 storm. The time of interest in this study was 16 September 2003, when the storm was over the open Atlantic near 27°N, 70°W. Vertical wind shear began increasing on 15 September, and by 16 September the storm weakened from category 3 to category 2. Figure 4b showed a strong downshear shift in this cirrus canopy associated with the vertical wind shear.

The G-IV flight track and the visible satellite image for Hurricane Isabel at 0945 UTC 16 September are given in Fig. 11. The major turbulence event in this flight was found near the core as the aircraft flew just outside of a partial eyewall northeast of the storm center. This period of strong turbulence, which began at 0908 UTC, will be examined further. A high-resolution plot of this turbulent region (Fig. 12) shows a bandedness in T_b northwest of the storm near the location of the one sonde (A) that was released in this region. Isabel contained several points where turbulence exceeded $3\,m\,s^{-2}$. Between the black asterisk and 70°W, 55.9% of points had turbulence above the 99th percentile, 4 times the frequency of the Ivan values in the outer bands. The largest turbulence along the track existed southeast of sonde A, just downwind of the convection located near the eyewall. The turbulent region also occurred downshear of the storm center (Fig. 4b), consistent with larger turbulence downshear overall (Fig. 6c). Variations in aircraft elevation associated with strong turbulence show clearly on this high-resolution plot. The aircraft elevation peaked at the end of the updraft as the vertical acceleration passed through zero, and was lowest at the end of the downdraft period, as expected. Time between vertical acceleration maxima ranged between 36 and 48 s southeast of sonde A, giving a time scale for the turbulent fluctuation.

The sonde skew T diagram (Fig. 13) differed dramatically from the Hurricane Ivan sondes. A deep, saturated, near-moist adiabatic layer exhibited almost no directional vertical shear in the entire column. The 200-hPa absolute vorticity (Fig. 14) also varied sharply from the Ivan case. Absolute vorticity was positive and quite large, with values near $17 \times 10^{-5}\,s^{-1}$ in the most turbulent region. The large turbulence thus existed in a cyclonic and inertially stable region. The greatest turbulence occurred downwind of an intense convective cell in the partial eyewall with little turbulence observed upwind. The Hurricane Isabel case provides an example of inner-core turbulence likely forced by eyewall convection.

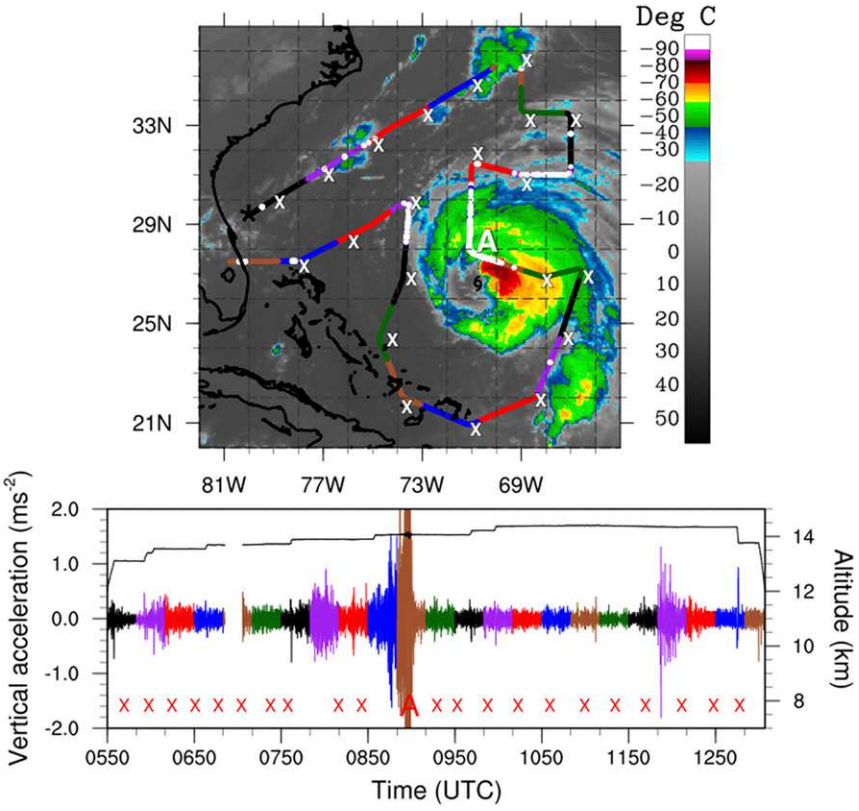

FIG. 11. As in Fig. 8, but for Hurricane Isabel at 0945 UTC 16 Sep 2003.

6. Discussion

a. Turbulence distribution

Both major hurricanes (greater than category 2) and weaker storms showed that turbulence within the inner 200 km of the radius was 35%–40% larger than at the outer radii, consistent with Duran and Molinari (2016; their Fig. 2), who found that the maximum low Richardson number frequency decreased monotonically with the radius over the same region. Major hurricanes exhibited about 8% larger turbulence than weaker storms at all radii. These expected results provide some verification of the value of the data, since deep convection on average is more frequent at small radii in strong hurricanes. More subtle aspects arose when the diurnal cycle and the role of the cirrus canopy were considered.

Overnight turbulence exceeded that during the day by 7%–9% over all radii. This surplus overnight increased to 22% if only the 200–400-km radii within the cirrus canopy were evaluated. This suggests that, as postulated by Bu et al. (2014), strong radiational cooling near the cirrus top overnight is playing a significant role in the enhancement of turbulence.

b. Case studies

The Hurricane Ivan case indicated a relationship between turbulence and outflow layer inertial instability, defined as absolute vorticity < 0. In principle, such local inertial instability can be removed by horizontal mixing; both inflow and outflow parcels accelerate in the same direction they are moving, eventually creating a neutral absolute angular momentum region analogous to the mixing of buoyant parcels in a heated boundary layer. As noted by Ooyama (1966), however, if the flow in the tropical cyclone is broadly outward, as seen in Fig. 10, then the acceleration in the unstable region would only be outward, creating strong outflow jets with potentially large vertical wind shear above and below. This type of structure was apparent in the wind fields at 175 hPa in Figs. 9 and 10, where air accelerated from the storm center into the inertially unstable region at larger radii. If parcel mixing by inflow and outflow cannot occur, inertial instability might require mixing on small vertical scales [Dunkerton (1983), who noted turbulence can be generated by the removal of inertial instability]. We hypothesize that the inertial instability came first as a result of interactions with westerlies. These interactions might also include the potential

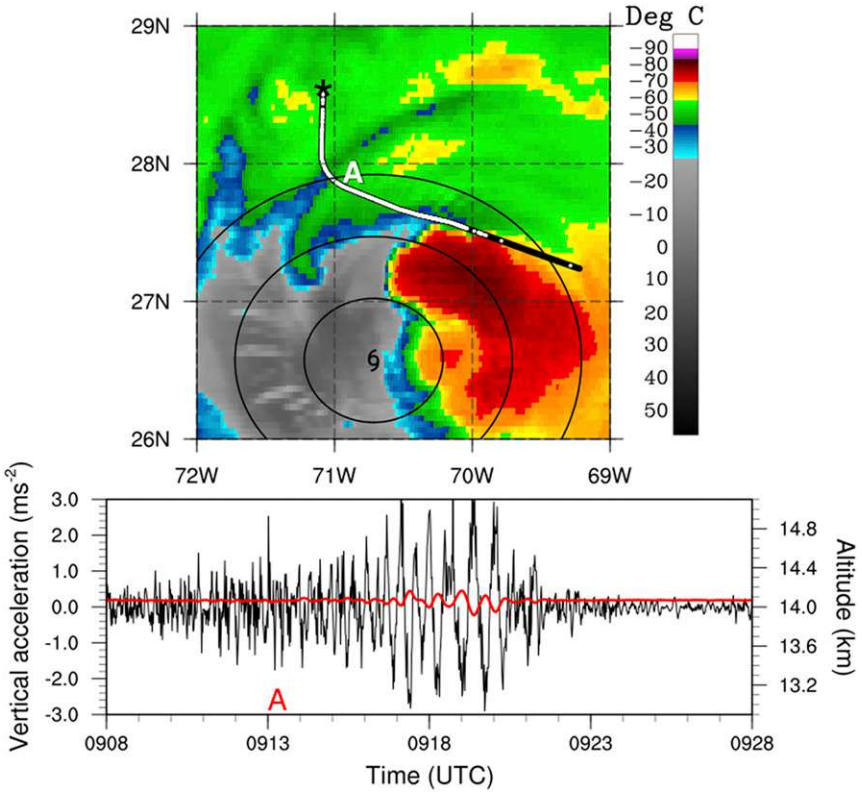

FIG. 12. As in Fig. 11, but highlighting the region containing the largest turbulence. (bottom) Turbulence (black) and aircraft altitude (red) over a 20-min period. Range rings are depicted at 50-km intervals. Only a single sonde ("A") was released in this region. The satellite image is valid at 0915 UTC 16 Sep 2003 to better coincide with the time of largest turbulence.

impact of negative absolute vorticity arising from the convection in the bands. Once the inertial instability developed, it was followed by acceleration of outflow, turbulence, and removal of instability on a 12-h time scale, which was suggested by Molinari and Vollaro (2014).

The sharp vertical gradients of outflow might play a critical role in the Hurricane Ivan turbulence. Figure 15 shows mean Richardson numbers during rapid intensification of a storm in an idealized axisymmetric simulation (adapted from Duran and Molinari 2019). The low Richardson number from 13- to 15-km elevation is consistent with the observations shown in Fig. 1. The tropical atmosphere in general has lower static stability at cirrus level, but this reduction in stability is much larger in hurricanes (Duran and Molinari 2016). Although the high-entropy narrow outflow has a positive static stability anomaly beneath it (not shown), the strong shear in the same layer and the offsetting effects of radiative cooling create low Richardson numbers in the upper troposphere (Duran and Molinari 2019). In addition, a narrow outflow channel can create shallow layers of inertial instability that contribute to the turbulence by reducing the absolute vorticity.

It is hypothesized that the sublimation near the 9-km level does not influence turbulence at the G-IV flight

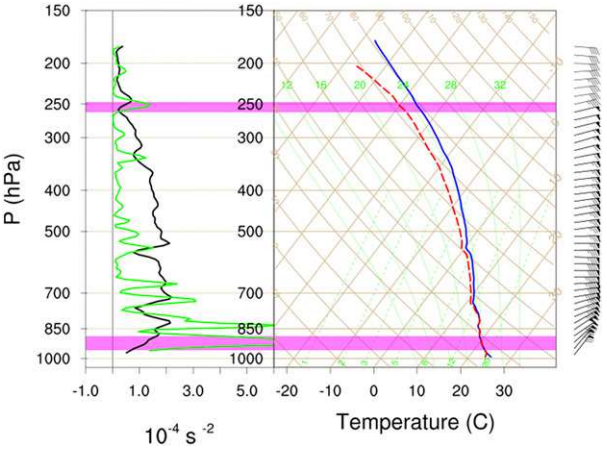

FIG. 13. As in Fig. 9, but for sonde A in Hurricane Isabel in Figs. 11 and 12, released at 0913 UTC 16 Sep 2003 at $r = 153$ km north-northwest of the storm center.

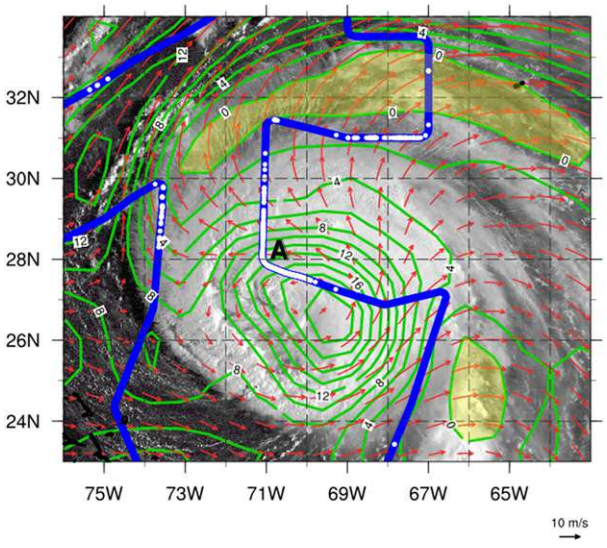

FIG. 14. As in Fig. 10, but for Hurricane Isabel at 1145 UTC 16 Sep. The absolute vorticity is from 1200 UTC. Unlike Fig. 10, the contour interval is $2 \times 10^{-5}\,s^{-1}$ with all values being shown.

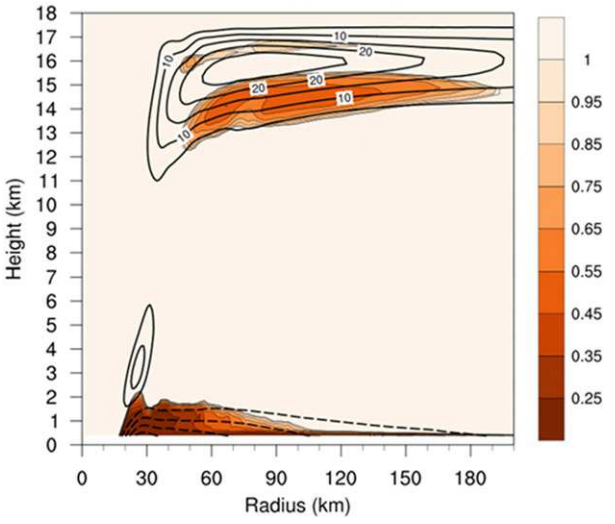

FIG. 15. Average over 24 h of rapid intensification from an axisymmetric Cloud Model 1 (CM1) numerical model (Bryan 2017; Bryan and Rotunno 2009) of radial velocity ($m\,s^{-1}$; contoured) and Richardson number (shaded). This figure was provided by Patrick Duran, adapted from the results of Duran and Molinari (2019).

level, because the turbulence extends only below cloud base. Nevertheless, such sublimation is likely indicative of strong outward advection of hydrometeors in enhanced outflow from the storm core, which could produce sublimation outside the core as these particles fall from the cirrus layer. It is hypothesized that the sublimation signature is an indicator of the existence of favorable conditions for turbulence beneath the cirrus, but is not a direct cause of turbulence at the G-IV flight level seen in this study.

The Hurricane Isabel case provided an example of turbulence near the core of a strong hurricane. Vertical acceleration varied sharply just downwind of intense convection in the eyewall. Turbulence values exceeded the 99th percentile of the flight-level dataset at more than 50% of data points in this region. Much smaller turbulence existed upwind of this convective feature. The time scale of this oscillation was 36–48 s yielding a wavelength of 8–12 km. Similar vertical velocity perturbations were seen just outside the core of Hurricane Patricia (Duran and Molinari 2018).

This region of turbulence was located downshear of the center in an area of large upper-tropospheric inertial stability. Absolute vorticity values approached $17 \times 10^{-5}\,s^{-1}$ in this region. This contrasted the region of turbulence in Hurricane Ivan, which was several hundred kilometers from the center of the storm and in an area with a history of inertial instability. It appears that, unlike Ivan, inertial instability played no apparent role in the generation of turbulence in the core of Isabel. Rather, it is hypothesized that the observed distribution of turbulence was generated by intense convection near the eyewall and advected downwind by the upper-level flow. The turbulence could have also been produced by convectively generated gravity waves that propagated northwestward.

The tropical cyclone outflow layer remains relatively unobserved. Duran and Molinari (2019) showed that enormous variations in tropopause-region static stability are driven primarily by (i) differential advection of entropy in both the horizontal and vertical and (ii) vertical gradients of radiative forcing and turbulence. A narrow layer of turbulence implied in Fig. 15 produces a well-mixed layer, but also produces stability maxima above and below where turbulence is not active. These turbulence-related stability changes alter the shape and strength of the radial–vertical circulation, especially in the upper troposphere.

7. Conclusions

The importance of turbulence in the tropical cyclone outflow layer addressed by Emanuel (2012) and Duran and Molinari (2019) provided the motivation for examining the only broad-based upper-level turbulence dataset available. The current study described a decrease in turbulence with radius and an increase with storm intensity. Nighttime values exceeded those in daytime. Turbulence outside the storm core was greatest within the cirrus canopy, suggesting the cloud-top cooling played a role. The case studies displayed the variable nature of the turbulent environment within the hurricane outflow layer:

low upper-tropospheric inertial stability and anticyclonic flow existed several hundred kilometers from the center at the edges of the cirrus canopy in Hurricane Ivan. High cloud was also present, suggesting a role for cirrus cloud-top cooling. In contrast, strong turbulence in Hurricane Isabel occurred at inner radii near deep eyewall convection in the presence of large absolute vorticity and inertial stability. The largest values were found downshear of the center and downwind of the upper-tropospheric flow from the eyewall.

Turbulence in the upper troposphere in a tropical cyclone can be generated in many ways. High-resolution simulations of tropical cyclones to further delineate the role of turbulence seem to be a promising avenue for further research.

Acknowledgments. We thank Dr. Robert Fovell of our department for helpful discussions of this work and for providing versions of Figs. 2 and 3 from Bu et al. (2014). Dr. Patrick Duran created Fig. 15. We express our appreciation to Dr. Jason Dunion of NOAA for pointing out the existence of the G-IV flight-level vertical acceleration data. Paul Flaherty (NOAA AOC) and Barry Damiano (retired) helped with processing of the data. This work is supported by NSF Grant AGS1636799.

APPENDIX

Removal of Artifacts in the Turbulence Data

Figure A1 shows the radial distribution of turbulence grouped into two sets of years. Also plotted is the standard deviation of turbulence for each group. It is apparent that one 6-yr period (2008–13) contained substantially larger turbulence (48%) versus the mean of the other years.

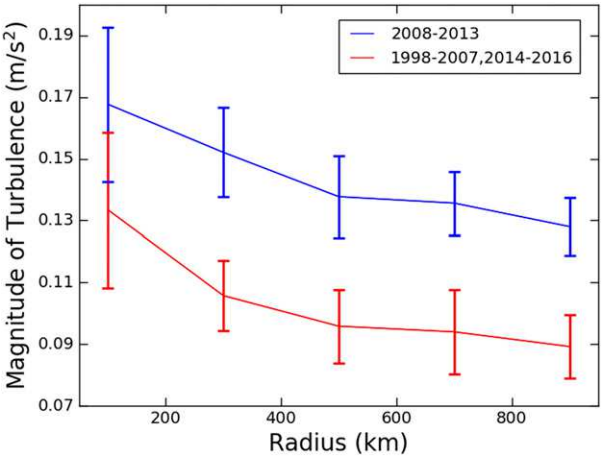

FIG. A1. Distribution of turbulence magnitude with radius for two sets of years: 2008–13 (blue lines) and 1998–2007 plus 2014–16 (red lines). The standard deviations of turbulence magnitude for each year for the two sets of data are given by the vertical lines.

TABLE A1. Mean values of several variables, comparing 2008–13 to all other years. The positive values for mean longitude refer to degrees west of the Greenwich meridian.

	2008–13	1998–2007 plus 2014–16
Mean turbulence magnitude ($m\,s^{-2}$)	0.144	0.0975
No. of data	1 552 891	3 407 923
Mean radius of data (km)	506	533
Mean altitude of data (km)	13.96	13.90
Mean latitude of data (°)	24.2	23.8
Mean longitude of data (°)	75.8	77.0
Mean maximum wind speed (kt)	67.1	78.8
Mean date	29 Aug	8 Sep

Table A1 compares storm and data distribution characteristics for these two periods. These periods do not meaningfully differ in the average radius and height of the data. There is also little difference in the mean location and time of year of the observed storms. The only appreciable difference is that the mean storm intensity was weaker by 11 kt for the period with larger turbulence. This result contradicts the findings of this paper that the magnitude of turbulence is positively correlated with storm intensity. Therefore, it appears that none of the analyzed characteristics could account for this change in turbulence magnitude.

Despite many communications with NOAA personnel, we could not track down the source of this discrepancy. We attribute the issue to a data processing problem, because persistent, multiyear INS errors of 50% are not possible. Two possible solutions existed: (i) omit the 6-yr outlier period, or (ii) normalize (i.e., reduce) the 2008–13 period to have the same mean as the other years. The normalization was chosen because the radial variation of turbulence (Fig. A1) was so similar for the two sets of data. This conservative approach allows us to use all years of data.

REFERENCES

Bryan, G. H., 2017: The governing equations for CM1. UCAR Tech. Note, 24 pp., http://www2.mmm.ucar.edu/people/bryan/cm1/cm1_equations.pdf.

——, and R. Rotunno, 2009: The maximum intensity of tropical cyclones in axisymmetric numerical model simulations. *Mon. Wea. Rev.*, **137**, 1770–1789, https://doi.org/10.1175/2008MWR2709.1.

Bu, Y. P., R. Fovell, and K. L. Corbosiero, 2014: Influence of cloud-radiative forcing on tropical cyclone structure. *J. Atmos. Sci.*, **71**, 1644–1662, https://doi.org/10.1175/JAS-D-13-0265.1.

Cairo, F., and Coauthors, 2008: Morphology of the tropopause layer and lower stratosphere above a tropical cyclone: A case study on cyclone Davina (1999). *Atmos. Chem. Phys.*, **8**, 3411–3426, https://doi.org/10.5194/acp-8-3411-2008.

Corbosiero, K. L., and J. Molinari, 2002: The effects of vertical wind shear on the distribution of convection in tropical cyclones. *Mon. Wea. Rev.*, **130**, 2110–2123, https://doi.org/10.1175/1520-0493(2002)130<2110:TEOVWS>2.0.CO;2.

Dee, D. P., and Coauthors, 2011: The ERA-Interim reanalysis: Configuration and performance of the data assimilation

system. *Quart. J. Roy. Meteor. Soc.*, **137**, 553–597, https://doi.org/10.1002/qj.828.

DeMaria, M., M. Mainelli, L. K. Shay, J. A. Knaff, and J. Kaplan, 2005: Further improvements to the Statistical Hurricane Intensity Prediction Scheme (SHIPS). *Wea. Forecasting*, **20**, 531–543, https://doi.org/10.1175/WAF862.1.

Dinh, T. P., D. R. Durran, and T. P. Ackerman, 2010: Maintenance of tropical tropopause layer cirrus. *J. Geophys. Res.*, **115**, D02104, https://doi.org/10.1029/2009JD012735.

Ditchek, S. D., J. Molinari, and D. Vollaro, 2017: Tropical cyclone outflow layer structure and balanced response to eddy forcings. *J. Atmos. Sci.*, **74**, 133–149, https://doi.org/10.1175/JAS-D-16-0117.1.

Dunkerton, T. J., 1983: A nonsymmetric equatorial inertial instability. *J. Atmos. Sci.*, **40**, 807–813, https://doi.org/10.1175/1520-0469(1983)040<0807:ANEII>2.0.CO;2.

Duran, P. D., and J. Molinari, 2016: Upper-tropospheric low Richardson number in tropical cyclones: Sensitivity to cyclone intensity and the diurnal cycle. *J. Atmos. Sci.*, **73**, 545–554, https://doi.org/10.1175/JAS-D-15-0118.1.

——, and ——, 2018: Dramatic inner-core tropopause variability during the rapid intensification of Hurricane Patricia (2015). *Mon. Wea. Rev.*, **146**, 119–134, https://doi.org/10.1175/MWR-D-17-0218.1.

——, and ——, 2019: Tropopause evolution in a rapidly intensifying tropical cyclone: A static stability budget analysis in an idealized, axisymmetric framework. *J. Atmos. Sci.*, **76**, 209–229, https://doi.org/10.1175/JAS-D-18-0097.1.

Emanuel, K. A., 2012: Self-stratification of tropical cyclone outflow. Part II: Implications for storm intensification. *J. Atmos. Sci.*, **69**, 988–996, https://doi.org/10.1175/JAS-D-11-0177.1.

——, and R. Rotunno, 2011: Self-stratification of tropical cyclone outflow. Part I: Implications for storm structure. *J. Atmos. Sci.*, **68**, 2236–2249, https://doi.org/10.1175/JAS-D-10-05024.1.

Kim, J.-H., H.-Y. Chun, R. D. Sharman, and S. B. Trier, 2014: The role of vertical shear on aviation turbulence within cirrus bands of a simulated western Pacific cyclone. *Mon. Wea. Rev.*, **142**, 2794–2813, https://doi.org/10.1175/MWR-D-14-00008.1.

Knox, J. A., A. S. Bachmeier, W. M. Carter, J. E. Tarantino, L. C. Paulik, E. N. Wilson, G. S. Bechdol, and M. J. Mays, 2010: Transverse cirrus bands in weather systems: A grand tour of an enduring enigma. *Weather*, **65**, 35–41, https://doi.org/10.1002/wea.417.

Kudo, A., 2013: The generation of turbulence below midlevel cloud bases: The effect of cooling due to sublimation of snow. *J. Appl. Meteor. Climatol.*, **52**, 819–833, https://doi.org/10.1175/JAMC-D-12-0232.1.

Kuester, M. A., M. J. Alexander, and E. A. Ray, 2008: A model study of gravity waves over Hurricane Humberto (2001). *J. Atmos. Sci.*, **65**, 3231–3246, https://doi.org/10.1175/2008JAS2372.1.

Landsea, C. W., and J. L. Franklin, 2013: Atlantic hurricane database uncertainty and presentation of a new database format. *Mon. Wea. Rev.*, **141**, 3576–3592, https://doi.org/10.1175/MWR-D-12-00254.1.

Lane, T. P., R. D. Sharman, S. B. Trier, R. G. Fovell, and J. K. Williams, 2012: Recent advances in the understanding of near-cloud turbulence. *Bull. Amer. Meteor. Soc.*, **93**, 499–516, https://doi.org/10.1175/BAMS-D-11-00062.1.

Lenz, A., K. M. Bedka, W. F. Feltz, and S. A. Ackerman, 2009: Convectively induced transverse band signatures in satellite imagery. *Wea. Forecasting*, **24**, 1362–1373, https://doi.org/10.1175/2009WAF2222285.1.

Luce, H., T. Nakamura, M. K. Yamamoto, and M. Yamamoto, 2010: MU radar and Lidar observations of clear-air turbulence underneath cirrus. *Mon. Wea. Rev.*, **138**, 438–452, https://doi.org/10.1175/2009MWR2927.1.

Melhauser, C., and F. Zhang, 2014: Diurnal radiation cycle impact on the pregenesis environment of Hurricane Karl (2010). *J. Atmos. Sci.*, **71**, 1241–1259, https://doi.org/10.1175/JAS-D-13-0116.1.

Molinari, J., and D. Vollaro, 2014: Symmetric instability in the outflow layer of a major hurricane. *J. Atmos. Sci.*, **71**, 3739–3746, https://doi.org/10.1175/JAS-D-14-0117.1.

——, P. Duran, and D. Vollaro, 2014: Low Richardson number in the tropical cyclone outflow layer. *J. Atmos. Sci.*, **71**, 3164–3179, https://doi.org/10.1175/JAS-D-14-0005.1.

Nolan, D. S., and J. A. Zhang, 2017: Spiral gravity waves radiating from tropical cyclones. *J. Geophys. Res. Lett.*, **44**, 3924–3931, https://doi.org/10.1002/2017GL073572.

Ooyama, K., 1966: On the stability of the baroclinic circular vortex: A sufficient condition for instability. *J. Atmos. Sci.*, **23**, 43–53, https://doi.org/10.1175/1520-0469(1966)023<0043:OTSOTB>2.0.CO;2.

Pfister, L., and Coauthors, 1993: Gravity waves generated by a tropical cyclone during the STEP tropical field program: A case study. *J. Geophys. Res.*, **98**, 8611–8638, https://doi.org/10.1029/92JD01679.

Rappin, E. D., M. C. Morgan, and G. J. Tripoli, 2011: The impact of outflow environment on tropical cyclone intensification and structure. *J. Atmos. Sci.*, **68**, 177–194, https://doi.org/10.1175/2009JAS2970.1.

Sharman, R. D., S. B. Trier, T. P. Lane, and J. D. Doyle, 2012: Sources and dynamics of turbulence in the upper troposphere and lower stratosphere: A review. *Geophys. Res. Lett.*, **39**, L12803, https://doi.org/10.1029/2012GL051996.

Thompson, G., P. R. Field, R. M. Rasmussen, and W. D. Hall, 2008: Explicit forecasts of winter precipitation using an improved bulk microphysics scheme. Part II: Implementation of a new snow parameterization. *Mon. Wea. Rev.*, **136**, 5095–5115, https://doi.org/10.1175/2008MWR2387.1.

Trier, S. B., and R. D. Sharman, 2009: Convection-permitting simulations of the environment supporting widespread turbulence within the upper-level outflow of a mesoscale convective system. *Mon. Wea. Rev.*, **137**, 1972–1990, https://doi.org/10.1175/2008MWR2770.1.

——, ——, R. G. Fovell, and R. G. Frehlich, 2010: Numerical simulation of radial cloud bands within the upper-level outflow of an observed mesoscale convective system. *J. Atmos. Sci.*, **67**, 2990–2999, https://doi.org/10.1175/2010JAS3531.1.

Vonich, P. T., and G. J. Hakim, 2018: Hurricane kinetic energy spectra from in situ aircraft observations. *J. Atmos. Sci.*, **75**, 2523–2532, https://doi.org/10.1175/JAS-D-17-0270.1.